Research Article

Lars Loetgering*, Max Rose, David Treffer, Ivan A. Vartanyants, Axel Rosenhahn and Thomas Wilhein

Data compression strategies for ptychographic diffraction imaging

https://doi.org/10.1515/aot-2017-0053
Received August 10, 2017; accepted October 10, 2017; previously published online November 18, 2017

Abstract: Ptychography is a computational imaging method for solving inverse scattering problems. To date, the high amount of redundancy present in ptychographic data sets requires computer memory that is orders of magnitude larger than the retrieved information. Here, we propose and compare data compression strategies that significantly reduce the amount of data required for wavefield inversion. Information metrics are used to measure the amount of data redundancy present in ptychographic data. Experimental results demonstrate the technique to be memory efficient and stable in the presence of systematic errors such as partial coherence and noise.

Keywords: diffraction imaging; phase retrieval; ptychography.

1 Introduction

Ptychographic coherent diffraction imaging (PCDI) and Fourier ptychographic microscopy (FPM) have emerged as computational imaging methods for the solution of inverse problems and phase retrieval in electron, X-ray, and visible light microscopy [1–3]. While PCDI has become popular for experiments where the use of high-quality optics is challenging [4, 5], FPM allows for space-bandwidth product extrapolation beyond the resolution limit in visible light imaging [6]. In its original conception, PCDI utilizes a fully coherent, localized illumination profile to produce scattered intensities from a spatially translated sample [7]. In practice, systematic errors hinder the ability for information recovery from the collected data sets, and the underlying inverse problem becomes ill posed. Current developments in the fields of PCDI and FPM aim at generalizing simple forward scattering models and compensating for departures from the aforementioned idealization. Recent advances include the incorporation of partial coherence [8–11], beam instabilities [12], scan position errors [13, 14], and statistical models for photoelectric counting distributions [15]. However, despite these successes, ptychography requires highly redundant data, typically orders of magnitude larger than the recovered information [16]. Moreover, the theoretically unlimited field of view in ptychography is practically limited by computational memory capacity. This complication limits the practical application of ptychography to moderate and high-computing facilities. In this paper, we investigate compression strategies for ptychographic diffraction imaging. Two compression strategies are proposed based on constrained sums and truncated singular value decomposition of diffraction data. The methods are tested and compared by numerical simulation and experiment.

2 Theory

This section reviews the elements of the theory of partially coherent light and describes the compression techniques underlying the simulation and experimental results described below.

***Corresponding author: Lars Loetgering,** Institute for X-Optics, RheinAhrCampus, Joseph-Rovan-Allee 2, 53424 Remagen, Germany, e-mail: lars.loetgering@fulbrightmail.org
Max Rose: Deutsches Elektronen-Synchrotron DESY, Notkestraße 85, 22607 Hamburg, Germany
David Treffer and Thomas Wilhein: Institute for X-Optics, RheinAhrCampus, Joseph-Rovan-Allee 2, 53424 Remagen, Germany
Ivan A. Vartanyants: Deutsches Elektronen-Synchrotron DESY, Notkestraße 85, 22607 Hamburg, Germany; and National Research Nuclear University MEPhI (Moscow Engineering Physics Institute), Kashirskoe Shosse 31, 115409 Moscow, Russia
Axel Rosenhahn: Analytical Chemistry – Biointerfaces, Ruhr-University Bochum, 44780 Bochum, Germany

2.1 Ptychography with partially coherent illumination

Partially coherent illumination in the space-time domain ($\boldsymbol{r}_1$, $\boldsymbol{r}_2$, t) represents the scalar electromagnetic wave field $E(\boldsymbol{r}, t)$ by the mutual degree of coherence [17],

$$\Gamma(\boldsymbol{r}_1, \boldsymbol{r}_2, \tau) = \int \bar{E}(\boldsymbol{r}_1, t) E(\boldsymbol{r}_2, t+\tau) dt, \tag{1}$$

where $\boldsymbol{r}_1$, $\boldsymbol{r}_2 \in \mathbb{R}^2$ denote spatial variables, $\tau \in \mathbb{R}$ denotes time-shift, and the bar (here and in the following) denotes complex conjugation. Alternatively, the cross-spectral density (CSD), defined by the relation

$$W(\boldsymbol{r}_1, \boldsymbol{r}_2, \omega) = \frac{1}{2\pi} \int \Gamma(\boldsymbol{r}_1, \boldsymbol{r}_2, \tau) e^{i\omega\tau} d\tau \tag{2}$$

in the space-frequency domain ($\boldsymbol{r}_1$, $\boldsymbol{r}_2$, ω), is more conveniently used than the mutual degree of coherence for two reasons. First, the CSD may be expanded into an infinite series [18]

$$W(\boldsymbol{r}_1, \boldsymbol{r}_2, \omega) = \sum_l \lambda_l(\omega) \bar{U}_l(\boldsymbol{r}_1, \omega) U_l(\boldsymbol{r}_2, \omega), \tag{3}$$

of orthonormal modes U_l, where λ_l are eigenvalues of the integral equation

$$\int W(\boldsymbol{r}_1, \boldsymbol{r}_2, \omega) U_l(\boldsymbol{r}_1, \omega) d^3\boldsymbol{r}_1 = \lambda_l(\omega) U_l(\boldsymbol{r}_2, \omega). \tag{4}$$

Equation (3) may be well approximated by a finite number of summation terms L if the scalar wavefield exhibits some degree of correlation. This assumption holds true for any type of electromagnetic radiation as long as the source plane is not concerned, as correlation is introduced in any wavefield upon propagation as a consequence of the Van-Cittert Zernike theorem [19]. From a computational point of view, the memory requirements, therefore, drastically decrease as the five-dimensional description of the CSD reduces to a finite number of two-dimensional modes and their corresponding energies. Second, the individual modes of the CSD obey a pair of Helmholtz equations [20], which allows to propagate the modes individually in numerical diffraction problems. The purity is a spatial coherence measure defined by [21]

$$\nu = \frac{\sqrt{\sum_l \lambda_l^2(\omega)}}{\sum_l \lambda_l(\omega)} \in [0, 1]. \tag{5}$$

Compared to other possible measures of partial transverse coherence [22], Equation (5) has the advantage that for a finite number of L equally weighted modes, we have $L = 1/\nu^2$ [23]. Therefore, $1/\nu^2$ can be interpreted as the effective number of modes needed to describe a partially coherent beam of purity ν. Note that in this case the purity is minimal. Hence, for L unequally weighted modes, $1/\nu^2$ may serve as an upper bound for the effective number of modes needed to numerically represent a partially coherent beam. In what follows, we are concerned with monochromatic scalar wavefields and, henceforth, drop the dependence on ω. Ptychographic implementations for polychromatic radiation are described in Refs. [9] and [10]. Further information on the spatial coherence properties of synchrotron and X-ray free electron lasers (XFELs) are found in Ref. [24].

In a ptychography experiment with optically thin objects [4], each exit-surface mode (ESM) $\psi_{\boldsymbol{x},l}$ ($l = 1, 2, \ldots, L$) can be modeled by the product

$$\psi_{\boldsymbol{x},l} = P_l(\boldsymbol{r}) O(\boldsymbol{r} - \boldsymbol{x}) \tag{6}$$

where $\boldsymbol{x} \in \mathbb{R}^2$ denotes the sample translation, O describes the complex-valued sample transmission function, and P_l is the l^{th} orthogonal mode in the illumination beam, usually referred to as *probe* in the context of ptychography. The intensities measured on a detector placed in the far field are modeled as an incoherent superposition of the spatial Fourier transforms of each individual ESM, i.e.

$$I_{\boldsymbol{x}} = \sum_l |\mathcal{F}\psi_{\boldsymbol{x},l}|^2. \tag{7}$$

Recovery of the ESMs $\psi_{\boldsymbol{x},l}$ from the set of measurements $I_{\boldsymbol{x}}$ is a nonlinear inverse problem that may be solved by iterative algorithms. Let $\psi^n_{\boldsymbol{x},l}$ describe an estimate for the l^{th} ESM with sample translation $\boldsymbol{x}$ at the n^{th} iteration. An improved estimate of $\psi^n_{\boldsymbol{x},l}$ complying with Equation (8) is then given by [8]

$$\psi^{n+1}_{\boldsymbol{x},l} = \mathcal{F}^{-1}\left(\sqrt{I_{\boldsymbol{x}}} \frac{\mathcal{F}\psi^n_{\boldsymbol{x},l}}{\sqrt{\sum_{l'} |\mathcal{F}\psi^n_{\boldsymbol{x},l'}|^2}} \right). \tag{8}$$

After satisfying the far-field intensity constraint, the updated ESMs $\psi^{n+1}_{\boldsymbol{x},l}$ are used to improve estimates of the probe modes and the object estimate to satisfy the ptychographic overlap constraint. This may be done using the difference map or the extended ptychographic iterative engine (ePIE) update rules described in Refs. [4] and [25], respectively. Finally, the probe modes have to be orthogonalized in accordance with the cross-spectral density being Hermitian [Equation (2)]. Various orthogonalization methods such as Gram-Schmidt orthogonalization, QR decomposition, and singular-value decomposition (SVD) may be used [26]. In the ptychographic reconstructions described below, we decompose the set of probe modes using a rank-L SVD, i.e.

$$\mathcal{P} = \mathcal{U}\mathcal{S}\bar{\mathcal{V}}, \tag{9}$$

where $\mathcal{P} = [P_1 | P_2 | \dots | P_L] \in \mathbb{C}^{N\times L}$, $\mathcal{U} \in \mathbb{C}^{N\times L}$, $\mathcal{S} \in \mathbb{R}^{L\times L}$, $\mathcal{V} \in \mathbb{C}^{L\times L}$, and N is the number of samples in a discretized wave of finite extent. It is noted that the SVD of $\mathcal{P}$ is compatible with Equation (4). This is readily seen adapting a finite-dimensional linear algebra point of view [22]. Assume a finite number of probe modes L, and write Equation (4) in matrix notation

$$W = U\Lambda\bar{U}, \tag{10}$$

where $W \in \mathbb{C}^{N\times N}$, $U \in \mathbb{C}^{N\times L}$, and $\Lambda \in \mathbb{C}^{L\times L}$. Then comparing Equation (10) and

$$\mathcal{P}\bar{\mathcal{P}} = \mathcal{U}\mathcal{S}^2\bar{\mathcal{U}}, \tag{11}$$

it is seen that $\mathcal{U}\mathcal{S}$ provides an orthogonal basis for $\mathcal{P}$ that is unique up to a constant complex phase factor $\exp[i\phi]$, a trivial non-uniqueness typically encountered in phase retrieval problems. In the ptychography implementation described below, the mode orthogonalization step is done via

$$\mathcal{P}^{n+1} = \mathcal{U}^n\mathcal{S}^n, \tag{12}$$

where $\mathcal{P}^n = [P_1^n | P_2^n | \dots | P_L^n] = \mathcal{U}^n\mathcal{S}^n\bar{\mathcal{V}}^n$ is the set of probe mode estimates and its SVD at the n^{th} iteration. Equations (10) and (11) are related by a similarity transformation depending on the basis in which the signals are represented, and we can identify $\lambda_l = \sigma_l^2$. In words, orthogonalization of a set of probe mode estimates by means of singular-value decomposition allows for interpreting the singular values as the square root of the energy contained in each respective mode. If the purity of the beam is unknown, L may be chosen sufficiently large, and a rank minimization algorithm may be used to find the effective degree of coherence [27, 28].

2.2 Information metrics

To compare the amount of information reduction in the original and compressed data, we define the compression

$$C = \frac{b_1}{b_0} \in [0, 1], \tag{13}$$

where b_0 and b_1 are the number of bytes in the uncompressed and compressed data sets, respectively. This metric is related to the redundancy

$$R = 1 - C. \tag{14}$$

The ptychographic oversampling σ [29] is defined as

$$\sigma = \frac{M\,(\text{pixels per diffraction pattern})}{2\,(\text{pixel in specimen} + \text{pixel in probe mode} \times L)} \tag{15}$$

where M is the number of diffraction patterns measured, and L is the effective number of modes, which depend on the purity as specified by Equation (5). Here, the effective ptychographic oversampling

$$\sigma_{\text{eff}} = \sigma C \tag{16}$$

is used to quantify the effective amount of sampling. In particular, we refer to $\sigma_{\text{eff}} \geq 1$ as conventional ptychography and to $\sigma_{\text{eff}} < 1$ as compressive ptychography.

2.3 Compression based on singular value decomposition

A ptychographic data set consists of multiple diffraction patterns related to the windowed Fourier transform of the sample [30]. It has been suggested that for pinhole illuminations in PCDI, the scanning step should be chosen in a way such that the linear overlap parameter between scan positions is above 60% [31]. This implies that diffraction intensities from neighboring and overlapping scan positions are typically correlated according to the ptychographic oversampling. Moreover, many samples are sparse or periodic in the spatial domain or contain homogeneous regions for which the diffraction intensities do not significantly change. In this case, the diffraction data becomes linearly dependent (low rank). In both cases, correlation or low rank, the data matrix can be approximated by a singular value decomposition. We therefore investigate to use singular value decomposition-based compression (SVDC) for PCDI data sets. The method treats each diffraction intensity in the uncompressed ptychographic data set as a column of a rectangular data matrix $D = [I_{\mathbf{x}_1} | \dots | I_{\mathbf{x}_M}] \in \mathbb{R}^{N\times M}$, where the number of detector pixels, N, is much larger than the number of scan positions, M. The SVDC method achieves data compression by means of a truncated SVD, i.e.

$$D \approx USV^\dagger, \tag{17}$$

where $U \in \mathbb{R}^{N\times K}$, $S \in \mathbb{R}^{K\times K}$, and $V \in \mathbb{R}^{M\times K}$ is a rank $K < M \ll N$ approximation of the full rank SVD of D. It is noted that U and V can be chosen real as D is real. The SVDC compression rate is

$$C = \frac{b_1}{b_0} = \frac{MK + K^2 + NK}{MN} \approx \frac{K}{M}. \tag{18}$$

2.4 Compression based on constrained pixel sums

In the same way that incoherent superpositions of exit surface modes can be discriminated using Equation (8), further modification of the denominator allows to separate other incoherent sums, for instance, as a consequence of binning. Reduction of diffraction data by summation over given regions S is referred to here as constrained pixel sum compression (CPSC). The method is described as follows (see Figure 1): all pixels p belonging to a region S in the original intensity I are summed up to form a pixel in a downsampled intensity I_s. In PCDI, this constraint can be used to modify an exit wave mode by the update rule

$$\psi_{\boldsymbol{x},l}^{n+1} = \mathcal{F}^{-1}\left(\sqrt{I_s}\frac{\mathcal{F}\psi_{\boldsymbol{x},l}^{n}}{\sqrt{\sum_{p\in S}\sum_{l'}|\mathcal{F}\psi_{\boldsymbol{x},l'}^{n}|^2}}\right). \tag{19}$$

The compression achieved by this method is given by $C = 1/|S|$, where $|S|$ denotes the number of pixels that belong to the region S. In the presence of sufficient data redundancy, this method principally allows for the recovery of the original intensity I from its downsampled version I_s. In contrast, binning leads to integration over finite detector areas, a decoherence effect present in any diffraction intensity but amplified through binning. Therefore, CPSC is not identical to binning as not the pixels in S, but only their sums are constrained, similar to Sudoku. Moreover, the method can be implemented with any partition of the original intensity domain, and $|S|$ does not have to be constant, in general. In this paper, we will explore only the extreme case of random summation with constant $|S|$ to demonstrate the method's generality.

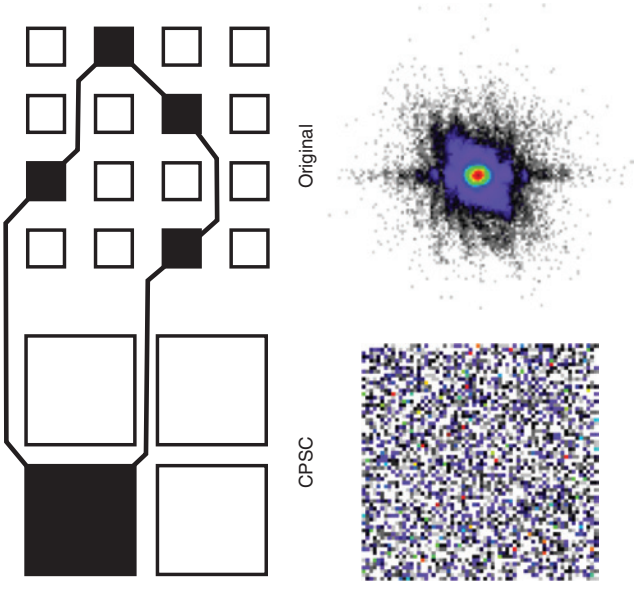

Figure 1: Constrained pixel sum geometry. (Top) The original data; (bottom) the downsampled signal from a sum over randomized pixel locations.

2.5 Resolution assessment

Resolution measures the spatial frequency response of an imaging system and, as such, is a measure of quality. Instead of giving a single-valued resolution metric, it is more precise to quantify resolution as a function of spatial frequency, as aberrations, noise, and systematic errors such as misalignment affect the entire spatial frequency response of an imaging system. The resolution of coherent and incoherent lens-based imaging systems is typically quantified by the amplitude and optical transfer function (ATF and OTF), respectively [32]. For lensless imaging systems, where specimen information is recovered by means of computational methods, closely related to the ATF and OTF is the Fourier ring correlation (FRC) given by

$$FRC(q_i) = \frac{\sum_{\boldsymbol{q}\in q_i}\tilde{O}_1^{*}(\boldsymbol{q})\,\tilde{O}_2(\boldsymbol{q})}{\sqrt{\sum_{\boldsymbol{q}\in q_i}|\tilde{O}_1(\boldsymbol{q})|^2\sum_{\boldsymbol{q}\in q_i}|\tilde{O}_2(\boldsymbol{q})|^2}}, \tag{20}$$

where $\boldsymbol{q}\in\mathbb{R}^2$ denotes spatial frequency, and the summations range over concentric rings of radius q_i. $\tilde{O}_k(\boldsymbol{q}) = \mathcal{F}O(\boldsymbol{r})$, $k = 1, 2$, are Fourier transforms of object reconstructions from two independent data sets. In this way, the FRC measures reproducibility of spatial frequency content as a normalized correlation of two signals. The intersection between the FRC and a 1-bit information threshold curve is defined as the resolution of the reconstructed object. This is referred to as the 1-bit criterion, which indicates the spatial frequency, as a fraction of the theoretical maximum (Nyquist limit), at which the reconstructed signal-to-noise ratio (SNR) is one. It has been noted that the 1-bit criterion, in practice, yields overly conservative resolution estimates, so for experimental data, the 1/2 bit criterion is typically used to assess resolution [33]. Because the FRC may exhibit oscillatory behavior, and thus many intersections with the 1/2-bit curve, we alternatively use the area under curve (AUC) defined by

$$\mathrm{AUC} = \sum_{q_i}\mathrm{FRC}(q_i), \tag{21}$$

as a resolution measure. If the spatial frequency response drops in the low or mid spatial frequency range, the 1/2-bit criterion is not sensitive to such changes, whereas the AUC detects information loss over the entire spatial frequency range.

3 Simulation

We performed numerical simulations to test the SVDC and CPSC compression strategies, both individually and in combination. To this end, six ptychographic data sets with varying compression rates ($C^{\mathrm{SVDC}}=1, 0.5, 0.25$; $C^{\mathrm{CPSC}}=1, 0.25$) were generated as summarized in Table 1. All data sets were assumed to be recorded on a detector with a dynamic range of 14 bit causing Poisson noise given by Mandel's formula [20] according to which the probability of recording n photoelectric counts given a time-integrated intensity $\int Idt$ is described by the probability density

$$p(n|I)=\frac{\int I^n dt}{n!}\exp\left(-\int Idt\right) \tag{22}$$

resulting in an average root mean square deviation compared to the noiseless data sets of 18%. A Gaussian-Schell model source was simulated using four Hermite-Gaussian probe modes [34] TEM_{00}, TEM_{10}, TEM_{01}, and TEM_{11} with a relative energy of 59.8%, 22%, 13.3%, and 4.9% resulting in a purity of 65%. The probes were cropped to not oversample the diffraction patterns, as this would allow for trivial compressibility of the data by conventional binning. The linear overlap parameter in the partially coherent data sets was 70%, which is larger than the proposed value of 60% in Ref. [31] to enable probe recovery with partial coherence. All reconstructions were obtained using an ePIE algorithm with 1000 iterations and a feedback parameter $\beta=0.5$ [25].

3.1 SVDC

The results for the SVDC simulation are shown in Figure 2 where the compression rate is indicated by red ($C^{\mathrm{SVDC}}=1$), green ($C^{\mathrm{SVDC}}=0.5$), and blue boxes ($C^{\mathrm{SVDC}}=0.25$). The visual similarity of the compressed reconstructions compared to the uncompressed reconstruction is in qualitative agreement. A quantitative analysis provided by the FRC curves shown at the bottom right of the top half of Table 1 summarizes the compression factors C^{SVDC}, the resolution as intersection with the 1/2 bit threshold, the AUC value, and the effective sampling σ_{eff}. As one would expect, the 1/2-bit resolution and AUC decrease slightly with increasing compression. The computational memory requirement decreases proportional to C^{SVDC} as indicated by σ_{eff}.

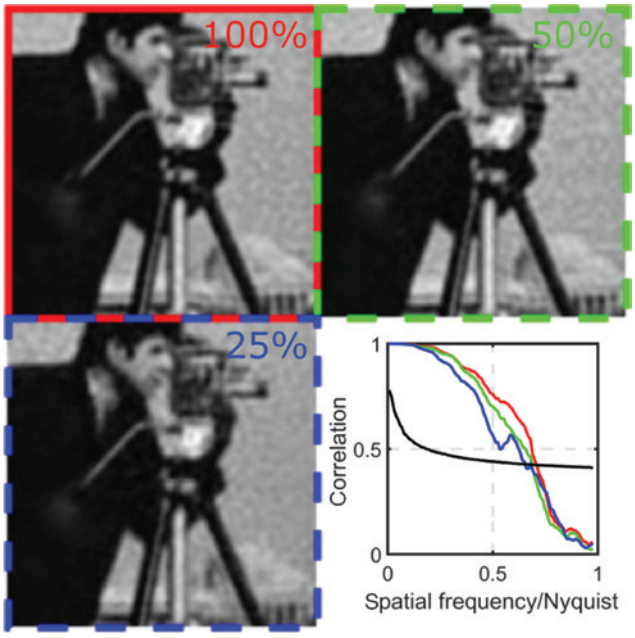

Figure 2: PCDI reconstruction for SVDC compression rates 100% (top left), 50% (top right), 25% (bottom left), and their FRC curves (bottom right) showing contrast vs. spatial frequency normalized to the Nyquist frequency.

Table 1: Resolution and AUC for various compression factors on simulated data.

C^{SVDC}	C^{CPSC}	1/2-bit resolution (%)	AUC (%)	σ_{eff}
1	1	70	66	7.6
0.5	1	66	62	3.8
0.25	1	65	60	1.9
1	0.25	61	56	1.9
0.5	0.25	58	55	1
0.25	0.25	48	49	0.5

Compressive ptychography with undersampling $\sigma_{\mathrm{eff}}<1$ was successfully realized with combinations of SVDC and CPSC.

3.2 CPSC

The results for the CPSC simulation with random binning ($C^{\mathrm{CPSC}}=1/|S|=0.25$) are shown in Figure 3, where the colored boxes indicate results when an additional SVD compression is used. The FRC curves with CPSC in Figure 3 show decreased reconstruction quality compared to the pure SVDC without binning (Figure 2). The quantitative analysis for the CPSC is summarized in the lower half of Table 1. It is important to note that the reconstructed object with $C^{\mathrm{CPSC}}=0.25$ and $C^{\mathrm{SVDC}}=0.25$ in the blue box has an effective oversampling smaller than unity. In this regard, these reconstructions are compressive in that they are obtained from a smaller number of data points than degrees of freedom in the object and probe modes reconstructed. This point is further discussed below.

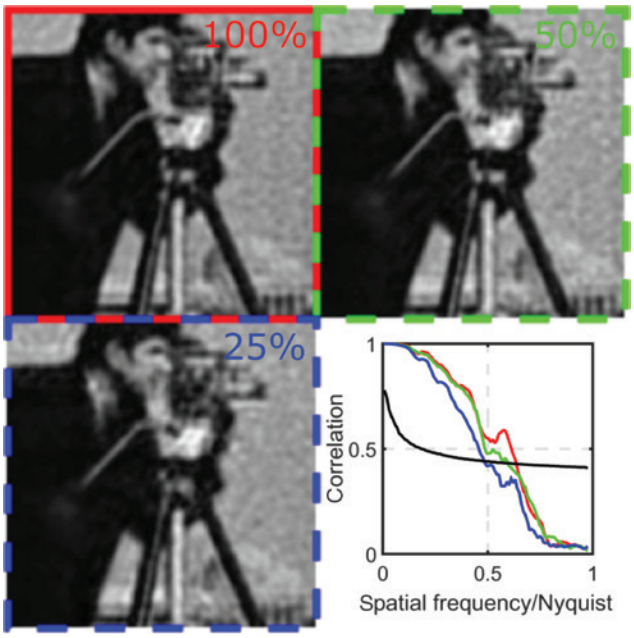

Figure 3: PCDI reconstruction and FRC curves for CPSC random binning ($C^{\mathrm{CPSC}} = 1/|S| = 25\%$) and SVDC compression (colored boxes). The diffraction patterns were binned as shown in Figure 1B.

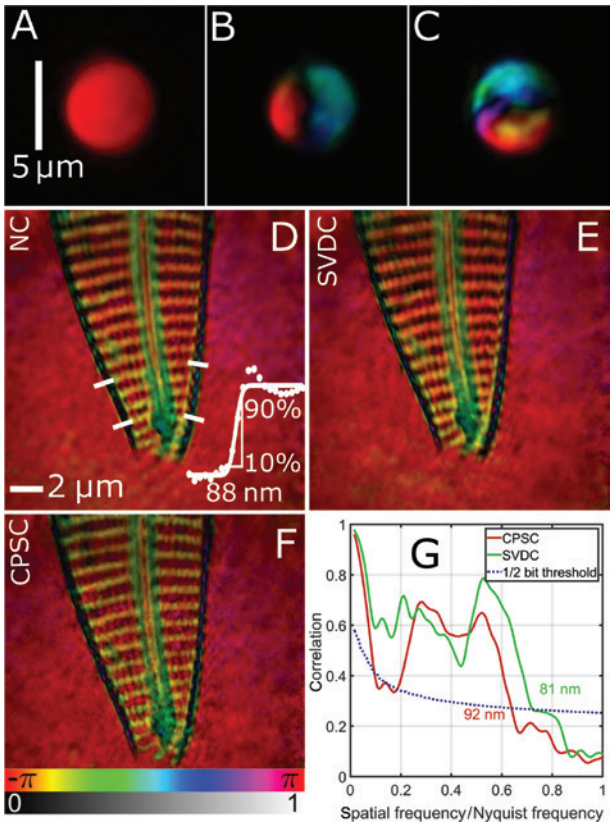

Figure 4: Compression results for experimental data. The colorbars (bottom) show relative phase shift (hue) and transmission (brightness) of the probe/sample. (A, B, C) The reconstructed modes TEM_{00}, TEM_{01}, and TEM_{10}, respectively, in the pinhole plane. The reconstructed diatom for no compression (NC), SVDC 50%, and CPSC 25% are shown below (D, E, F). (G) The FRC curves for the compressed reconstructions compared to the uncompressed reconstruction.

4 Experimental results (diatom)

Experimental data was collected at the soft X-ray beamline P04 of the PETRA III storage ring [35]. The APPLE-II type undulator was tuned to generate photons with energy of 500 eV ($\lambda = 2.48$ nm), i.e. close to the oxygen K absorption edge. A spectral bandwidth of 25 meV was selected by an exit slit opening of 25 µm of the monochromator. For this spectral bandwidth, the expected temporal coherence was about 50 µm. A focused beam with full width at half maximum (FWHM) of 15 µm in both directions was spatially filtered by a pinhole with a 5-µm diameter. The photon flux behind the pinhole was about 700 photons/s. Compared to a previous experiment with a twice smaller pinhole diameter [36], a similar photon flux at three times smaller X-ray bandwidth was obtained due to a newly added horizontal focusing mirror. The measurements were performed in the HORST (holographic roentgen scattering) vacuum chamber in the PCDI mode [37]. The PCDI data set was measured at a distance of 16 cm in the far field. To image an area of 20 µm × 25 µm on the sample, 86 scan positions arranged on a Fermat spiral [38] with an average linear overlap of 60% between the illumination positions were scanned. The detector was a back-illuminated and Peltier cooled (−60°C) CCD image sensor (DODX436-BN, Andor Technology Ltd., Belfast, UK). The square detector area of 27.6 mm × 27.6 mm consisted of 2048 pixels with a pixel size of 13.5 µm × 13.5 µm. The diffraction data was cropped to an effective detector size of 6.8 mm × 6.8 mm, resulting in a reconstruction pixel size (Nyquist resolution) of 58.3 nm. The specimen examined was a diatom with an exoskeleton consisting of silicon dioxide (SiO_2). The diatom skeleton was dispersed on a silicon nitride (Si_3N_4) membrane and air dried for the measurement under vacuum.

PCDI reconstructions for the diatom with varying compression rates are shown in Figure 4. The top row shows $L = 1/\nu^2 \approx 3$ reconstructed probe modes of the beam, for which a purity of $\nu = 59.5\%$ was estimated. Panels D, E, and F show the diatom reconstruction with no compression (NC), SVD compression (SVDC), and constrained pixel sum compression (CPSC). The resolution of the uncompressed reconstruction was estimated by averaging the resolutions for four-edge scan as indicated by the white lines in panel D. The line was fitted by an integrated Gaussian profile with an average FWHM of 80 nm and an average 10%–90% amplitude increase within an interval of 88 nm. From these values, we estimate the uncompressed reconstruction to have a resolution on the order of 80–90 nm. The SVDC result in panel E was obtained with a compression rate of $C^{\mathrm{SVDC}} = 0.5$ ($\sigma_{\mathrm{eff}} \approx 3.1$). The CPSC result in F was obtained with $C^{\mathrm{CPSC}} = 0.25$ ($\sigma \approx 1.5$). Higher compression rates were tested for both methods but resulted in increasingly visible artifacts. Panel G shows Fourier ring correlation curves for the reconstructions in panels E and F compared with panel D. We emphasize that, the compressed reconstructions were correlated with the Fourier transform of the uncompressed reconstruction and not, as customary, with a reconstruction from two independent data sets. We chose this procedure to facilitate comparison of reconstruction quality for varying degrees of compression within the same data set. The resulting FRC curves indicate that the SVDC method with a compression rate of 0.5 resulted in a half-bit resolution (half period) of 81 nm. The CPSC method with a compression

rate of 0.25 achieved a half-bit resolution (half period) of 92 nm. Visually inspecting the reconstruction results in Figure 4, panel E shows only minor differences compared to panel D, in agreement with the comparable resolution values attributed to these images. Panel E, in contrast, clearly shows artifacts such as ringing at the specimen edge and reduced contrast in the horizontal structures of the diatom.

5 Discussion

The SVD compression described in this paper and the discrete cosine transform (DCT), which underlies the lossy encoding step in JPEG compression [39], are compared in Figure 5. Panel A shows the uncompressed average diffraction pattern, also termed power spectral density (PSD), as used for the simulations in Section 3. Panels B and C show the PSDs obtained for the DCT and SVD compression methods. While the DCT compression method finds a suitable intra-frame basis for 8×8 pixel blocks, the SVD achieves inter-frame compression by finding the least square approximation for a truncated basis of the whole data set. The superiority of the SVD-based compression

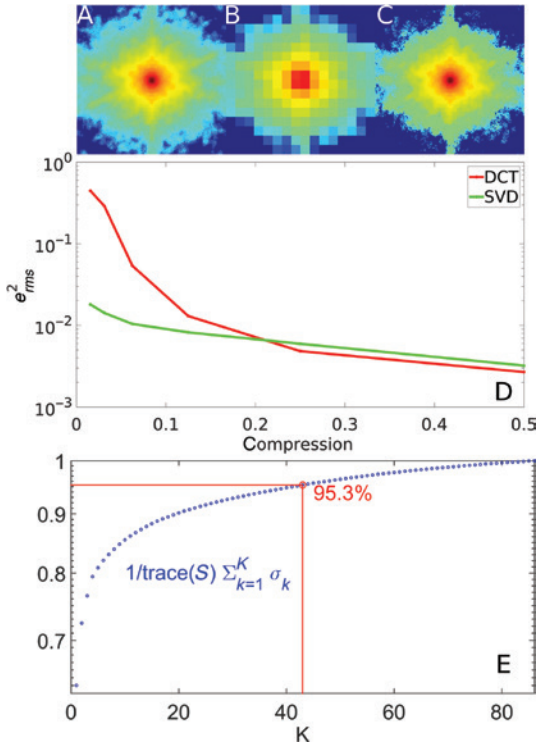

Figure 5: Original power spectral density (A) compared to DCT (B) and SVD (C) compression for a compression rate of 3% applied to the simulated data in Figure 2. (D) Mean square deviation of DCT (red) and SVD (green) compression from original data set for various compression rates. (E) Percentage of the truncated SVD coefficients compared to the trace of the full rank SVD. Half of the full rank SVD describes 95.3% of the diatom data set.

over the DCT-based compression is quantified by the mean square deviation shown in Panel D. For comparison, the lossless PNG format could only obtain a compression of about 70% due to the noise in the data.

The success of the compression methods proposed here strongly depends on the object under investigation. However, there are criteria to identify data compressibility. For example, periodic specimen such as lithographic masks and integrated circuits [16, 40] result in PCDI scans with repeating diffraction patterns when adequately scanned. The SVDC method can take advantage of this periodicity by finding a lower dimensional basis to represent the data in. In other words, the data matrix is not full rank and, thus, is singular. In practice, however, the data contains noise so the SVDC method has to filter out the principal components of the data matrix. In the experiment reported here, the data could be reduced by 50% without sacrificing significant resolution. Tests with higher compression rates resulted in noticeable artifacts. If there is no *a priori* knowledge about the specimen, compressibility by means of the SVDC method can be identified by inspection of the singular values of the data matrix as depicted in Figure 5E for the diatom data set. Here, the original rank-86 data matrix is approximated by a rank-43 truncated SVD, whereby the singular values of the latter sum up to 95.3% of the former. The normalized root mean square error of the SVDC approximation for the diatom data is given by [see Equation (17)]

$$|| D - USV^{\dagger} ||_{rms} = \sqrt{\frac{1}{\mathrm{tr}(S^2)} \sum_{k=K+1}^{M} s_{k,k}^2} \approx 0.7\%, \tag{23}$$

where tr denotes trace, and $s_{k,k}$ are the diagonal elements of S.

Compressibility using the CPSC method depends on various factors such as the overlap in scan positions and the structure of the probe. It was demonstrated by Edo et al. [41] that undersampling the diffraction data may be compensated by increasing the overlap in the scan positions. The CPSC includes the possibility of binning neighboring pixels but allows for more general binning geometries while preserving the photon statistics of the original data. An interesting question for future research is how to construct suitable binning masks that achieve maximum compression. As a trivial example, if a given zero photon count region is binned, the constrained sum leaves no doubt about the individual pixels. Another implication of the CPSC method is that it may be applied in reverse, namely, if the sampling on the detector is too coarse; for instance, to resolve a small speckle, the CPSC method may be used to constrain upsampled data [42].

A difference between the SVDC and the CPSC should be mentioned. The former approximates the data, while the latter loses information about the data. Approximation of the data leads to systematic errors. We observed that these have a smaller effect when the ePIE algorithm is used in conjunction with small feedback parameters effectively leading to averaging various object estimates. The drawback is that this leads to slower convergence. Losing information about the data does not lead to inconsistencies due to systematic errors but may render the inverse problem ill posed. *A priori* knowledge such as sparsity [43] may be beneficial in such cases.

6 Summary and conclusion

We have demonstrated two novel compression strategies for ptychographic diffraction imaging. The proposed methods were tested by simulation and experiment. It is expected that data compression techniques will become relevant as coherent diffraction methods increase in complexity and computational demands. Last, shifting the focus from providing more information to filtering the relevant information will not only be beneficial in big data problems but also in small-scale devices such as portable Fourier ptychographic microscopes on cell phones [44].

Acknowledgment: L. Loetgering would like to thank M. Odstrcil and B. Kanngießer for helpful discussions. The authors greatly acknowledge the experimentalists (T. Senkbeil, A.V. Gundlach, S. Stuhr, and C. Rumancev) from Ruhr-University Bochum for their approval to test the compression strategies on their experimentally collected data. This research was supported by the research initiative Rhineland-Pfalz. We gratefully acknowledge the support of NVIDIA Corporation with the donation of the Tesla K40 GPU used for this research. L. Loetgering developed the compression theory, wrote the manuscript, and analyzed the simulation and experimental data. M. Rose reconstructed the experimental data. M. Rose, I. Vartanyants, D. Treffer, A. Rosenhahn, and T. Wilhein edited the manuscript.

References

[1] M. Humphry, B. Kraus, A. Hurst, A. Maiden and J. Rodenburg, Nat. Commun. 3, 730 (2012).
[2] J. M. Rodenburg, A. C. Hurst, A. G. Cullis, B. R. Dobson, F. Pfeiffer, et al., Phys. Rev. Lett. 98, 034801 (2007).
[3] G. Zheng, R. Horstmeyer and C. Yang, Nat. Photonics 7, 739–745 (2013).
[4] P. Thibault, M. Dierolf, A. Menzel, O. Bunk, C. David, et al., Science 321, 379–382 (2008).
[5] A. M. Maiden, G. R. Morrison, B. Kaulich, A. Gianoncelli and J. M. Rodenburg, Nat. Commun. 4, 1669 (2013).
[6] J. Holloway, Y. Wu, M. K. Sharma, O. Cossairt and A. Veeraraghavan, Sci. Adv. 3, e1602564 (2017).
[7] J. M. Rodenburg and H. M. L. Faulkner, Appl. Phys. Lett. 85, 4795–4797 (2004).
[8] P. Thibault and A. Menzel, Nature 494, 68–71 (2013).
[9] B. Enders, M. Dierolf, P. Cloetens, M. Stockmar, F. Pfeiffer, et al., Appl. Phys. Lett. 104, 171104 (2014).
[10] D. J. Batey, D. Claus and J. M. Rodenburg, Ultramicroscopy 138, 13–21 (2014).
[11] M. Odstrcil, J. Bussmann, D. Rudolf, R. Bresenitz, J. Miao, et al., Opt. Lett. 40, 5574–5577 (2015).
[12] M. Odstrcil, P. Baksh, S. A. Boden, R. Card, J. E. Chad, et al., Opt. Express 24, 8360–8369 (2017).
[13] A. M. Maiden, M. J. Humphry, M. C. Sarahan, B. Kraus and J. M. Rodenburg, Ultramicroscopy 120, 64–72 (2012).
[14] F. Zhang, I. Peterson, J. Vila-Comamala, A. Diaz, R. Bean, et al., Opt. Express 21, 13592–13606 (2013).
[15] P. Thibault and M. Guizar-Sicairos, New J. Phys. 14, 063004 (2012).
[16] M. Guizar-Sicairos, I. Johnson, A. Diaz, M. Holler, P. Karvinen, et al., Opt. Express 22, 14859 (2014).
[17] J. W. Goodman, in: 'Statistical Optics', 2nd edition (Wiley, New York, 2015).
[18] E. Wolf, J. Opt. Soc. Am. 72, 343–351 (1982).
[19] E. Wolf, in 'Introduction to the Theory of Coherence and Polarization of Light', (Cambridge University Press, Cambridge, 2007).
[20] L. Mandel and E. Wolf, in 'Optical Coherence and Quantum Optics', (Cambridge University Press, Cambridge, 1995).
[21] M. A. Alonso, Adv. Opt. Photonics 3, 272 (2011).
[22] H. M. Ozaktas, JOSA A 19, 1563–1571 (2002).
[23] A. Starikov, J. Opt. Soc. Am. 72, 1538–1544 (1982).
[24] I. A. Vartanyants and A. Singer, New J. Phys. 12, 035004 (2010).
[25] A. M. Maiden and J. M. Rodenburg, Ultramicroscopy 109, 1256–1262 (2009).
[26] W. H. Press, S. A. Teukolsky, W. T. Vetterling and B. P. Flannery, in: 'Numerical Recipes: The Art of Scientific Computing', 3rd edition (Cambridge University Press, Cambridge, 2007).
[27] L. Tian, J. Lee, S. B. Oh, and G. Barbastathis, Opt. Express 20, 8296 (2012).
[28] J. F. Cai, E. J. Candès, and Z. Shen, SIAM J. Optim. 20, 1956–1982 (2010).
[29] A. M. Maiden, M. J. Humphry, F. Zhang, and J. M. Rodenburg, J. Opt. Soc. Am. A 28, 604–612 (2011).
[30] R. Horstmeyer and C. Yang, Opt. Express 22, 338–358 (2014).
[31] O. Bunk, M. Dierolf, S. Kynde, I. Johnson, O. Marti, et al., Ultramicroscopy 108, 481–487 (2008).
[32] J. Goodman, in: 'Introduction to Fourier Optics', 3rd edition (Roberts and Company Publishers, Eaglewood, 2004).
[33] M. Van Heel and M. Schatz, J. Struct. Biol. 151, 250–262 (2005).
[34] I. A. Vartanyants and A. Singer, in: 'Coherence Properties of Third-Generation Synchrotron Sources and Free-Electron Lasers', 1st edition (Springer International Publishing, Switzerland, 2016).

[35] J. Viefhaus, F. Scholz, S. Deinert, L. Glaser, M. Ilchen, et al., Nucl. Instrum. Methods Phys. Res. Section A 710, 151–154 (2013).
[36] M. Rose, P. Skopintsev, D. Dzhigaev, O. Gorobtsov, T. Senkbeil, et al., J. Synchrotron Radiat. 22, 819–827 (2015).
[37] T. Gorniak and A. Rosenhahn, Z. Phys. Chem. 228, 1089–1104 (2014).
[38] X. Huang, H. Yan, R. Harder, Y. Hwu, I. K. Robinson, et al., Optimization of overlap uniformness for ptychography. Opt. Express 22, 12634 (2014).
[39] G. K. Wallace, IEEE Tran. Consum. Electron. 38, xviii–xxxiv (1992).
[40] M. Holler, M. Guizar-Sicairos, E. H. R. Tsai, R. Dinapoli, E. Müller, et al., Nature 543, 402–406 (2017).
[41] T. B. Edo, D. J. Batey, A. M. Maiden, C. Rau, U. Wagner, et al., Phys. Rev. A 87, 1–8 (2013).
[42] H. Froese, L. Lötgering and T. Wilhein, SPIE Opt. Optoelectron. 10233, 102331A1–102331A9 (2017).
[43] Y. Shechtman, Y. C. Eldar, O. Cohen, H. N. Chapman, J. Miao, et al., IEEE Signal Process. Mag. 32, 87–109 (2015).
[44] S. Dong, K. Guo, P. Nanda, R. Shiradkar and G. Zheng, Biomed. Opt. Express 5, 3305–3310 (2014).

Lars Loetgering
Institute for X-Optics, RheinAhrCampus, Joseph-Rovan-Allee 2, 53424 Remagen, Germany,
lars.loetgering@fulbrightmail.org

Lars Loetgering is currently enrolled as a PhD student at the Institute of X-Optics at the University of Applied Science, Koblenz. His research interests include computational imaging and inverse problems.

Max Rose
Deutsches Elektronen-Synchrotron DESY, Notkestraße 85, 22607 Hamburg, Germany

Max Rose is a PhD student at Deutsches Elektronen-Synchrotron in the group of Ivan A. Vartanyants. His research interests include coherent diffraction imaging via phase retrieval of biological specimen using synchrotron and FEL sources.

David Treffer
Institute for X-Optics, RheinAhrCampus, Joseph-Rovan-Allee 2, 53424 Remagen, Germany

David Treffer is a MSc student at the University of Applied Science, Koblenz. He is currently working at the Institute for X-Optics, Remagen.

Ivan A. Vartanyants
Deutsches Elektronen-Synchrotron DESY, Notkestraße 85, 22607 Hamburg, Germany
National Research Nuclear University MEPhI (Moscow Engineering Physics Institute), Kashirskoe Shosse 31, 115409 Moscow, Russia

Ivan A. Vartanyants is a leading scientist at the Deutsches Elektronen-Synchrotron DESY and a professor at the National Research Nuclear University MEPhI (Moscow Engineering Physics Institute). His research interests include coherent diffraction imaging, phase retrieval, analysis of coherence properties of synchrotron and FEL sources, and X-ray dynamical theory.

Axel Rosenhahn
Analytical Chemistry – Biointerfaces, Ruhr-University Bochum, 44780 Bochum, Germany

Axel Rosenhahn is a professor for Analytical Chemistry at Ruhr-University Bochum. He works on understanding biological processes at interfaces and develops new analytical tools including *in situ* X-ray imaging methods.

Thomas Wilhein
Institute for X-Optics, RheinAhrCampus, Joseph-Rovan-Allee 2, 53424 Remagen, Germany

Thomas Wilhein is a professor at the University of Applied Science, Koblenz. His research interests include high-resolution X-ray imaging with laboratory and synchrotron radiation sources.